RSC Advances

PAPER

View Article Online
View Journal | View Issue

Cite this: *RSC Adv.*, 2023, **13**, 21769

Novel sensor for the determination of CA 15-3 in serum of breast cancer patients based on Fe–gallic acid complex doped in modified cellulose polymer thin films†

Hind A. AlGhamdi,[a] Yasmeen M. AlZahrani,[a] Salha Alharthi,[a] Mohamed S. Mohy-Eldin,[b] Ekram H. Mohamed,[c] Safwat A. Mahmoud*[d] and Mohamed S. Attia*[e]

Fe–gallic acid MOF embedded in an epoxy methyl cellulose polymer (CMC) thin film was synthesized and characterized by different micro-analytical tools such as: FE-SEM/EDX, XPS analysis, XRD analysis, FT-IR, and fluorescence spectroscopy. Fe–gallic acid MOF doped in a stable CMC polymer thin film is used as a novel sensor to identify CA 15-3 in the sera of patients suffering breast malignancy. The presence of appropriate functional groups in aqueous CA 15-3 solutions enables it to interact with the Fe–gallic acid MOF embedded in the thin film. The Fe–gallic acid MOF was found to absorb energy at 350 nm (λ_{ex}) and emits radiation at 439 nm which was specifically quenched in the presence of CA 15-3 over a working concentration range of 0.05–570 U mL^{-1}. In contrast to other CA 15-3 detection methods which suffered from electronic noise, interference and slowness, the Fe–gallic acid MOF proved its sensitivity as an economic, stable and reliable probe for the detection and determination of CA 15-3 in patients' serum samples with a detection limit of 0.01 U mL^{-1} at pH 7.2.

Received 14th April 2023
Accepted 11th July 2023

DOI: 10.1039/d3ra02495d

rsc.li/rsc-advances

1. Introduction

The second-leading cause behind cancer-related death in women is known to be breast cancer; in addition it is the most frequently diagnosed cancer in women. Records from the literature have demonstrated that both current and past research has a significant impact on enhancing the clinical prognosis for breast cancer. This has been credited to the advancements in breast cancer management in the areas of screening, diagnosis, and therapeutic approaches. Yet, triple-negative breast cancer poor prognosis and medication resistance pose serious obstacles against the control of the disease. The increased incidence and mortality rates of breast cancer in the populations of developing countries are also considered a major source of worry.[1] The potential of treatment and hence the lower risk of death are significantly enhanced the earlier the malignancy is detected. Tumor markers' inadequate selectivity and sensitivity make them poor candidates to be employed as tools for early detection of breast cancer.[2] Mammograms, MRI images, screening for spectroscopic, and breast biopsies are widely used for decisive diagnosis of breast cancer. Unfortunately, these detection methods are expensive, time-consuming, and invasive, require surgery, and sometimes yield unsatisfactory results. Thus it is not feasible to apply these methods to track the effectiveness of treatment and whether the tumor is responding to the suggested management guidelines. Therefore, the demand for a sensitive and selective methods for fast monitoring the progress of breast cancer, its response to the treatment and metastasis is considered as a priority. CA 15-3 tumor marker could serve such function and could be used to screen the breast cancer recurrence, to assess how effectively the treatment is working and whether the tumor is shrinking or spreading (metastasis) in response to treatment. Recent studies revealed the diagnostic accuracy of CA 153 in case of breast malignancy surveillance.[3–5] Different techniques were used for estimating CA 153 including chemiluminescence immunoassays,[6] enzyme immunoassays,[7] radioimmunoassay (RIA),[8] electrochemical immunoassay,[9] photoelectrochemical immunoassay,[10] and immunosorbent enzyme-linked assays.[11] Nevertheless, the above methods struggle to fulfil the growing clinical needs for quick detection of CA 15-3 due to lengthy apheresis, complicated label collection, and other drawbacks.

[a]*Chemistry Department, College of Science, Imam Abdulrahman Bin Faisal University, P.O. Box 1982, Dammam 31441, Saudi Arabia*

[b]*Polymer Materials Research Department, Advanced Technology and New Materials Research Institute (ATNMRI), City of Scientifc Research and Technological Applications (SRTA-City), New Borg El-Arab City, P. O. Box: 21934, Alexandria, Egypt*

[c]*Analytical Chemistry Department, The British University in Egypt, El Sherouk city, Cairo 11378, Egypt*

[d]*Physics Department, Faculty of Science, Northern Border University, Arar, Saudi Arabia*

[e]*Chemistry Department, Faculty of Science, Ain Shams University, Abbassia, Cairo 11566, Egypt. E-mail: Mohamed_sam@yahoo.com*

† Electronic supplementary information (ESI) available. See DOI: https://doi.org/10.1039/d3ra02495d

Furthermore, tumor markers when present in very low concentration, cannot be detected with the above mentioned conventional methods, necessitating the hunt for novel strategies.[12] Metal–organic frameworks (MOFs) are crystalline porous materials with a high degree of both compositional and structural control. MOFs are composed of metal ions or groups coordinated with organic bonds forming one or multidimensional structures. MOFs have attracted much attention in the sensing field due to their advantages of porosity, large specific surface area, structural and functional diversity, and unsaturated metal sites.[13–17] The luminescence of MOFs can originate from the ligands, metal ions, or the interaction between ligands and metal ions. Many types of sensors are used, such as ZIF-8, ZIF-67, Ln-MOFs, and UiO-66. Although MOFs have been widely used for sensing, lanthanide metal ions and complex organic linkers are the main sources of their tunable fluorescence properties. This suggests that their synthesis will be extremely challenging.[18–21] In addition to the luminescence of the MOF itself, the luminescence of MOFs can be realized by introducing luminous guests into the metal–organic framework. Due to their structural properties, MOFs are an excellent class of hosts, and by adding guests, their variety of functions and practical applications can be modified. Using the porosity of MOF hosts to encapsulate various luminescent guests (LGs), thus forming LG@MOF composite systems, is a unique approach to obtaining luminescence from MOFs (LMOFs).[22–28] Over conventional syntheses of luminescent materials, guest encapsulation into MOFs has some benefits, including the simplicity and cost-effectiveness of this methodology, the possibility of tuning the emission properties by a rational selection of commercially available fluorophores or luminescent dyes, and the avoidance of aggregation-caused quenching (ACQ) phenomena, by partitioning of the luminescent guests into the pores of the crystalline MOF host. LG@MOFs not only combine the advantages of LGs and MOFs but also maintain the original morphological characteristics. The adsorption ability of MOFs makes the analyte concentrate near the fluorescence sensor, to improve the sensitivity. At the same time, the separation ability of MOFs extinguishes interfering substances, to improve the selectivity. The embedding of LGs, makes the optical characteristics of LG@MOFs more adjustable. In addition, the functional groups on the surface of the LG may be the binding sites of the target, which is helpful to improve its sensing performance. Therefore, combining the hybrid characteristics of MOFs and specific optical properties of LGs, for the preparation of LG@MOF composites, with complex pore structures and excellent optical properties, is a promising strategy to fabricate a new generation of fluorescent sensors. The aim of this study is developing a new method for quantifying CA 15-3 in serum of breast cancer women. CA 15-3 is a protein that is produced by breast cancer cells. It is often used as a tumor marker to monitor the progress of breast cancer. The new method developed by this study is based on the use of Fe–gallic acid doped in epoxy cellulose polymer metal–organic framework (MOF) complex. In this case, the MOF complex is able to capture and bind CA 15-3. The MOF complex is then incorporated into a thin film. The new method developed by this study has the potential to be a valuable tool for the diagnosis and monitoring of breast cancer. It is a simple, easy-to-use, and stable that is also cost-effective.

2. Materials and reagents

Gallic acid (trihydroxybenzoic acid), $C_6H_2(OH)_3CO_2H$, purity (99.0%) and ferric sulfate hydrate, $Fe_2(SO_4)_3 \cdot 5H_2O$, purity (97.0%) and carboxymethyl cellulose (CMC) were purchased from (Sigma Aldrich Chemicals Ltd., Germany). Epichlorohydrin, purity claimed to be 99.5% was purchased from (Sigma-Aldrich Chemie Gmbh, USA). All the chemicals used throughout the study were of analytical grade and were used directly with no need for any further purification. CEA, CA 19-9 and CA 125 were purchased from Mybiosource. Uric acid, urea and glucose were purchased from (Sigma Aldrich Chemicals Ltd., Germany). CA 15-3, MBS318280, 50 K units was purchased from (Mybiosource, USA).

2.1. Standard solution

CA 15-3 stock solution was prepared by dissolving the CA 15-3 antigen vial in 2 mL distilled water. Further dilutions were performed to obtain different concentrations of CA 15-3 using distilled water. All standard solutions were maintained at temperature 2–8 °C when are not in use.

2.2. Instruments

Double beam UV-vis spectrophotometer (model: Edinburgh Instruments DS5) equipped with a xenon flash lamp having a spectral range of 190–1100 nm. A spectrofluorometer (Edinburgh Instruments FS5) having a spectral range up to 1650 nm and fluorescence lifetimes down to 25 ps. A pH meter (model: Jenway-3040). A Daihan Scientific centrifuge device (model: CF-10). Fourier transform infrared (FTIR) (model: Shimadzu-FTIR-8400 S, Japan). Differential scanning calorimeter (model: Shimadzu DSC-50, Japan). Renishaw Raman (model:RM1000) equipped with the 532 nm laser line. Electrically refrigerated CCD camera, and a notch filter to eliminate the elastic scattering. Surface roughness tester (model: SJ-201P, Japan). The FE-SEM images and EDX spectroscopy spectra were recorded with a combination of field emission scanning electron microscopy (FE-SEM), and element mapping by spatially resolved energy-dispersive X-ray spectroscopy (EDX) (JEOL JSM-6510LV, Japan).

2.3. Preparation of modified polysaccharide

Three grams of carboxymethyl cellulose (CMC) was suspended in 100 mL water followed by the addition of 4 mL of epichlorohydrin. The activation process was conducted at 65 °C for 3 hours using a water bath. For promoting the reaction between hydroxyl groups of CMC and epichlorohydrin, dilute NaOH solution was added to maintain basic pH. After being allowed to cool, the solution was cast in a Petri dish and left for dryness overnight at 25 °C. Fig. 1.

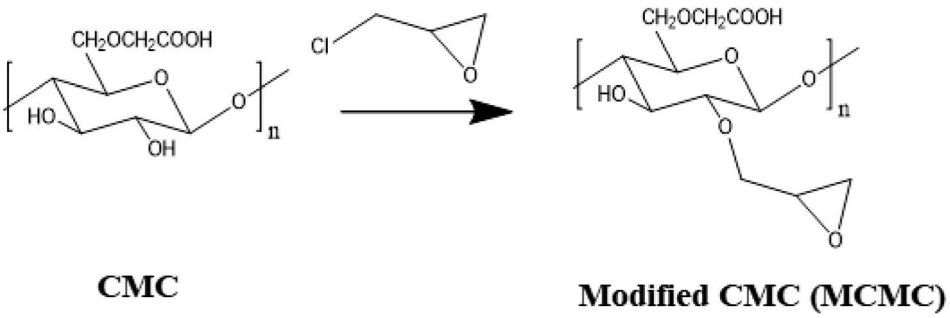

Fig. 1 Schematic preparation of epoxy-functionalized carboxymethyl cellulose.

2.4. Synthesis of Fe–gallic metal organic framework

The MOF synthesis was performed through a hydrothermal/solvothermal method in which; $Fe_2(SO_4)_3 \cdot 5H_2O$ (3.0 mmol, 1.470 g) dissolved in 50 mL distilled water/dimethylformamide (3 : 2, v/v), was added dropwise to a round flask containing 50 mL of gallic acid (1.0 mmol, 0.170 g) dissolved in distilled water, the acquired mixture was then transferred to a 150 mL thermal autoclave and left in the oven maintained at temperature 200 °C over 24 hours. The obtained reddish brown precipitate was filtrated and thoroughly washed using ethanol and distilled water.

2.5. Preparation of Fe–gallic acid MOF embedded in epoxy-functionalized carboxymethyl cellulose polymer thin film

The functionalizing epoxy cellulose polymer with epichlorohydrin has many advantages. (1) It improves the properties of the polymer, such as its solubility, wettability, or mechanical strength. (2) Adding a new functionality to the polymer, such as the ability to bind to other molecules or to respond to changes in the environment. (3) Functionalizing epoxy cellulose polymer with epichlorohydrin can be used to create new materials with specific properties, such as polymers that can be used in biomedical applications. In the case of the interaction between the CA 15-3 and Fe–gallic acid MOF that led to fluorescence quenching, the epichlorohydrin functionalization of the polymer is thought to play a role in two ways. The epichlorohydrin groups can facilitate the interaction of the CA 15-3 with the Fe–gallic acid MOF, which makes it easier to detect the presence of CA 15-3 by the quench of Fe–gallic acid MOF fluorescence intensity.

Step 1: for thin film preparation, functionalizing epoxy cellulose polymer with epichlorohydrin solution was mixed with the Fe–gallic acid in one container and agitated for 15 minutes. A spin coater operating at 500 rpm was used to manufacture the thin film.

Step 2: in the 1.0 cm fluorimeter cell, suitable volumes of different CA 15-3 samples prepared in distilled water were added and mixed with the previously fabricated thin film in step 1, Fig. 2.

2.6. General procedure

To study the effect of CA 15-3 on the absorption and emission spectra of optical sensor certain volume is taken from the CA 15-3 stock solution to prepare the required concentration in 10 mL volumetric flask and the volume was completed by distilled water. 1.5 mL of this concentration was added to the thin film doped Fe–gallic acid MOF in the fluorimetric cell. The emission spectrum was recorded at $\lambda_{ex}/\lambda_{em}$ = 350/439 using distilled water. The prepared optical sensor was utilized to measure the subsequent absorption and emission spectra. The spectra of luminescence were recorded at 350 nm (λ_{ex}). A washing solution was used to rinse the thin film between measurements.

2.7. Sample preparation

All samples were collected between october 2022 and march 2023 from the New Al-Kasr-EL-Aini Teaching Hospital Cairo University and Ain Shams Specialized Hospital, Ain shams University, Cairo, Egypt in accordance with the protocol approved by WHO (World Health Organization) for human specimen collection and the use of this material and related clinical information for research purposes [all patients consented and approved the use of their clinical samples in the research work].

All animal procedures were performed in accordance with the Guidelines for Care and Use of Laboratory Animals of "Faculty of Pharmacy, British University in Egypt" and experiments were approved by the Animal Ethics Committee of "Research Ethics Committee, (REC)". After a standard history and physical examination, blood was drawn for routine laboratory measures. Serum samples were collected from all the volunteers; (i) control subjects (10 samples), (ii) patients breast cancer (20 samples). 3.0 mL of citrate solution was added to 4.0 mL plasma and the solution was centrifuged for 15.0 min at 4000 rpm to remove all proteins. After decantation, 1.0 mL of the serum was added with 0.1 mL of the buffer (pH = 7.3) to the thin film embedded biosensor in the cuvette, and finally the 1.9 mL of water was added to give the test solution.

2.8. Proposed method

An appropriate amount (100 μL) of various standard concentrations of the CA 15-3 in water was mixed with the thin film doped Fe–gallic acid MOF in the cell. The fluorescence spectra were then recorded at the $\lambda_{ex}/\lambda_{em}$ = 350/439 nm. The thin film was rinsed with water after each measurement and the calibration plot was constructed by plotting $(F_0/F - 1)$ at λ_{em} = 439 nm on the

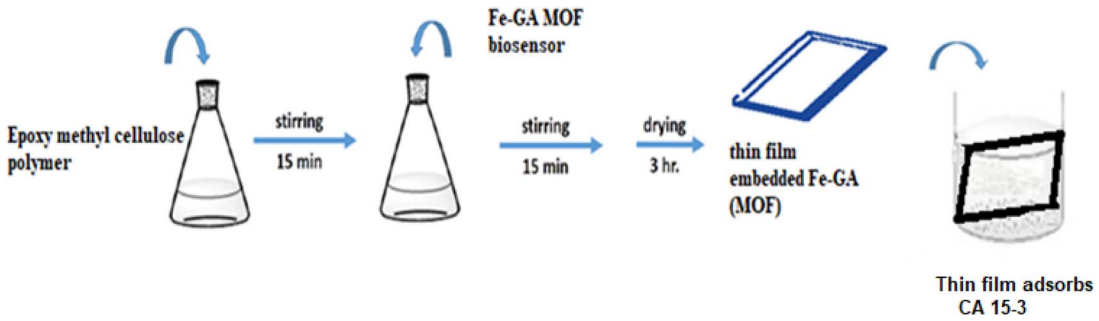

Fig. 2 Preparation of thin film containing biosensor embedded in epoxy cellulose polymer.

y axis against the CA 15-3 concentration on the *x* axis. The concentration of CA 15-3 was measured by withdrawing (100 μL) of each serum sample and completed to 3 mL by water in cell of the spectrofluorometer in presence of the thin film and then the emission intensity of the Fe–gallic acid MOF doped in epoxy cellulose polymer thin film was measured at 439 nm.

3. Results and discussion

Full characterization for all the components of the Fe–gallic acid MOF doped in epoxy cellulose polymer thin film was performed using most advanced characterization tools.

3.1. Characterization of the modified epoxy carboxymethyl cellulose polymer

The modified CMC membrane was characterized using FTIR, differential scanning calorimetry (DSC), Raman spectroscopy analysis as well as surface roughness tester to measure the surface roughness (ESI S1.1, 2,3,4†).

3.2. Characterization of Fe(III)–GA–MOF

After preparation of Fe(III)–GA–MOF using hydrothermal/solvothermal as detailed previously, the structure elucidation using the acquired qualitative and quantitative micro analytical tools was discussed herein below.

3.2.1. FE-SEM/EDX. The prepared Fe(III)–GA–MOF was imaged using FE-SEM at different magnifications and the obtained images were represented in (Fig. 3a–c). The morphology appears to be aggregates of broken brick blocks with a smooth surface. The upper surface is homogeneous and composed of small nanoparticles. While EDX analysis of Fe(III)–GA–MOF was presented in Fig. 3d. The data showed that the building blocks of its structure were oxygen, carbon, sulfur and iron. Fe(III)–GA–MOF formation was confirmed by mapping analysis displaying

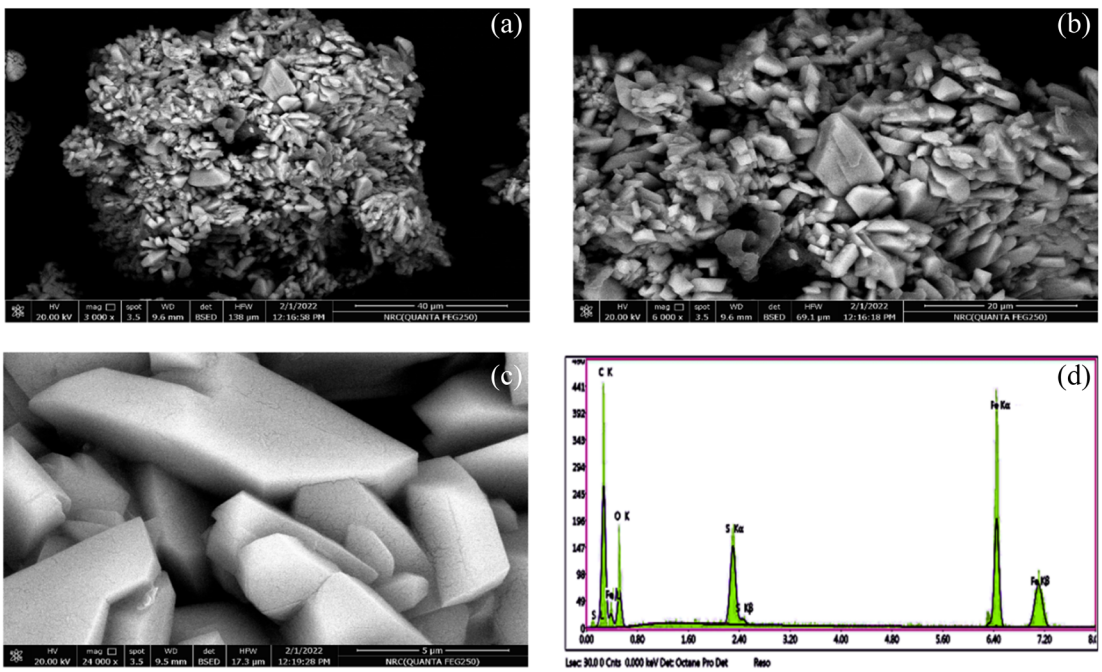

Fig. 3 (a–c) The field-emission scanning electron microscopy images of the ferric metal–organic framework (Fe(III)–GA–MOF) at different magnification, and (d) energy-dispersive X-ray analysis with a single point EDX mapping analysis of Fe(III)–GA–MOF.

the party elements massive dispersion as presented in Fig. 3d. The CMC elemental structure activation with epichlorohydrin is presented in Fig. 4a. The increase in oxygen, carbon and chloride concentrations altered the elemental composition of the integrated biosensor, as shown in Fig. 4b. Upon CA 15-3 antibody immobilization and it reacted with CA 15-3, the concentration of carbon increased while that of oxygen and chloride decreased in the favor of nitrogen. The alteration of the elemental composition represented in Fig. 4c confirmed the antibody immobilization. The elemental composition transformations were also reflected on the surface morphology. Fig. 4a and b revealed the change of CMC with epichlorohydrin surface from particle to compact layer structure. The surface roughness of the CMC films read 0.183 ± 0.053 μm, compared

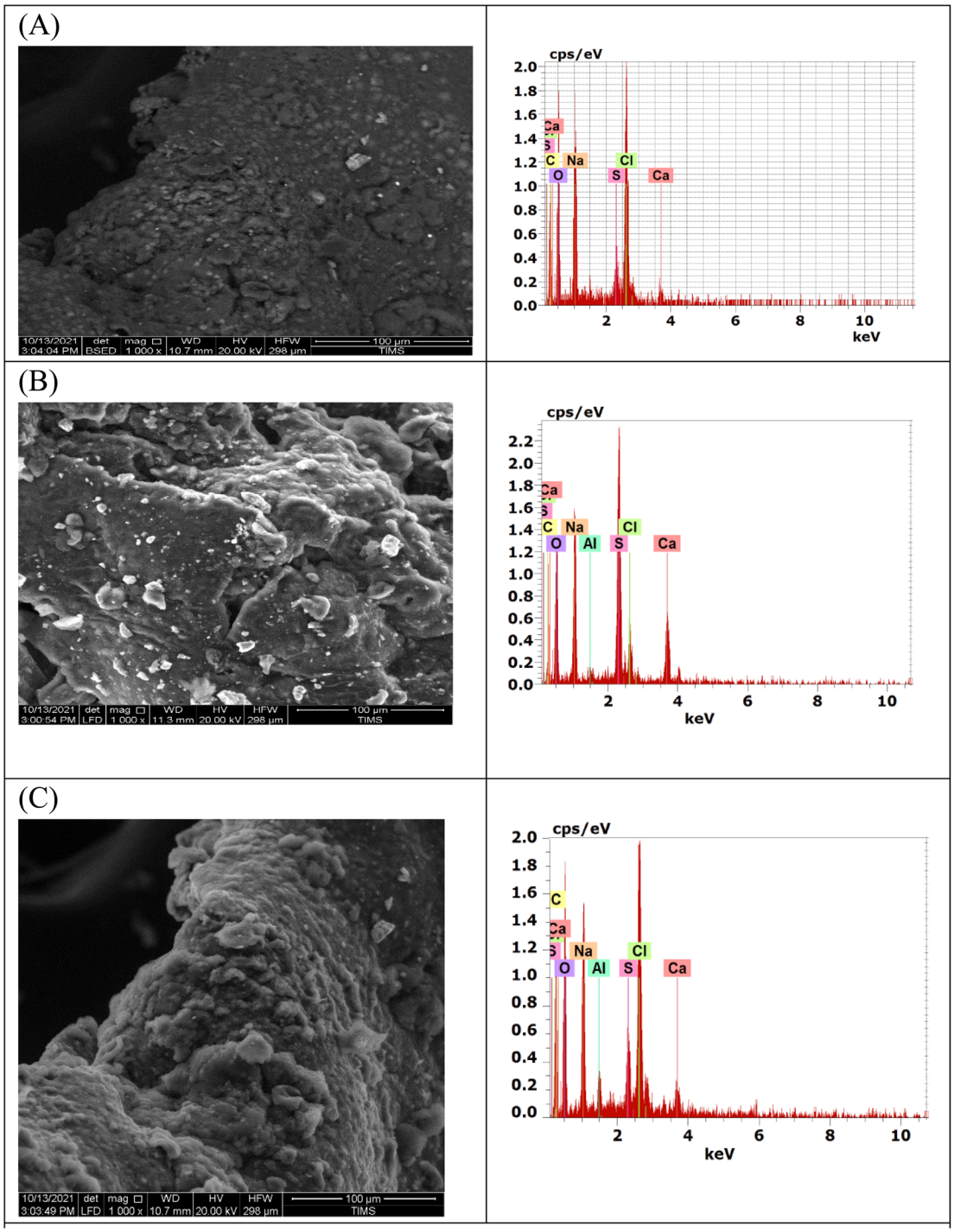

Fig. 4 SEM image of epoxy CMC thin film (A), epoxy CMC embedded Fe–gallic MOF thin film (B), and epoxy CMC embedded Fe–gallic MOF + monoclonal antibody CA 15-3 thin film (C).

to 0.428 ± 0.064 μm for the modified CMC membrane. A significant increase in the surface roughness of the epoxy functionalized membranes was found. The presence of new groups along the polymer chains affected the arrangement of the molecules during the casting process, which led to a perturbation of the crystal arrangement and the formation of structural films with a rough surface.[29] Immobilized CA 15-3 antibody interaction with CA 15-3 created a coating layer which led the surface profile to be smoother as shown in Fig. 4c.

3.2.2. XPS analysis. The Fe(III)–GA–MOF chemical components was characterized using XPS, Fig. 5. The four main spectral parts of this sample were analyzed using the XPS wide spectral survey. The XPS scan presented in Fig. 5a and S2.1† exhibited clearly detected peaks of iron (Fe 2p), oxygen (O 1s), carbon (C 1s) and sulfur (S 2p). Fe 2p peak was deconvoluted into six spectral peaks as shown in Fig. 5b and S2.2.† The six spectral peaks were observed at binding energies of 710.66, 714.38, 718.14, 723.96, 725.59 and 728.24 eV, due to Fe $2p_{1/2}$ and Fe $2p_{3/2}$, for Fe(III) and Fe(II). The most abundant Fe(III) satellite peaks at 710.66 eV and 723.96 eV which confirmed the Fe^{3+} extinction of Fe(III) $2p_{3/2}$ and Fe(III) $2p_{1/2}$, respectively with a decreasing energy difference of 13.3 eV.[30] Fig. 5c and S2.3† presented the spectrum of the detuned O 1s peaks at 531.73, 532.69 and 533.12 eV.[31] Fig. 5d and S2.4† show the C 1s region, with spectral peaks at 288.60, 286.38 and 284.75 eV assigned to C=O, C=C and C–O respectively.[32] Finally, Fig. 5e and S2.5† present the S 2p spectrum and it shows one peak at 168.89 eV due to the presence of sulfur in the sample. ESI S2.6† contained more detailed information about XPS analysis.

3.2.3. XRD analysis. The spectrum pattern of Fe(III)–GA–MOF XRD was represented in Fig. 5f. The XRD patterns show sharp peaks in the MOFs confirming that the crystalline phase of the material is formed. Moreover, the main peaks in the Fe(III)–GA–MOF diffraction pattern are observed at values of 2θ of about 9.24°, 11.84°, 16.8°, 20.10°, 23.00°, 26.5°, 29.88°, 56.44°, 58.63° and 61.45°. Details of the list of peaks of the XRD analysis of Fe(III)–GA–MOF are presented in ESI S2.7.† In addition, the diffraction pattern of Fe(III)–GA–MOF was in good agreement with that of the MOF-based gallic structure.[33a,b]

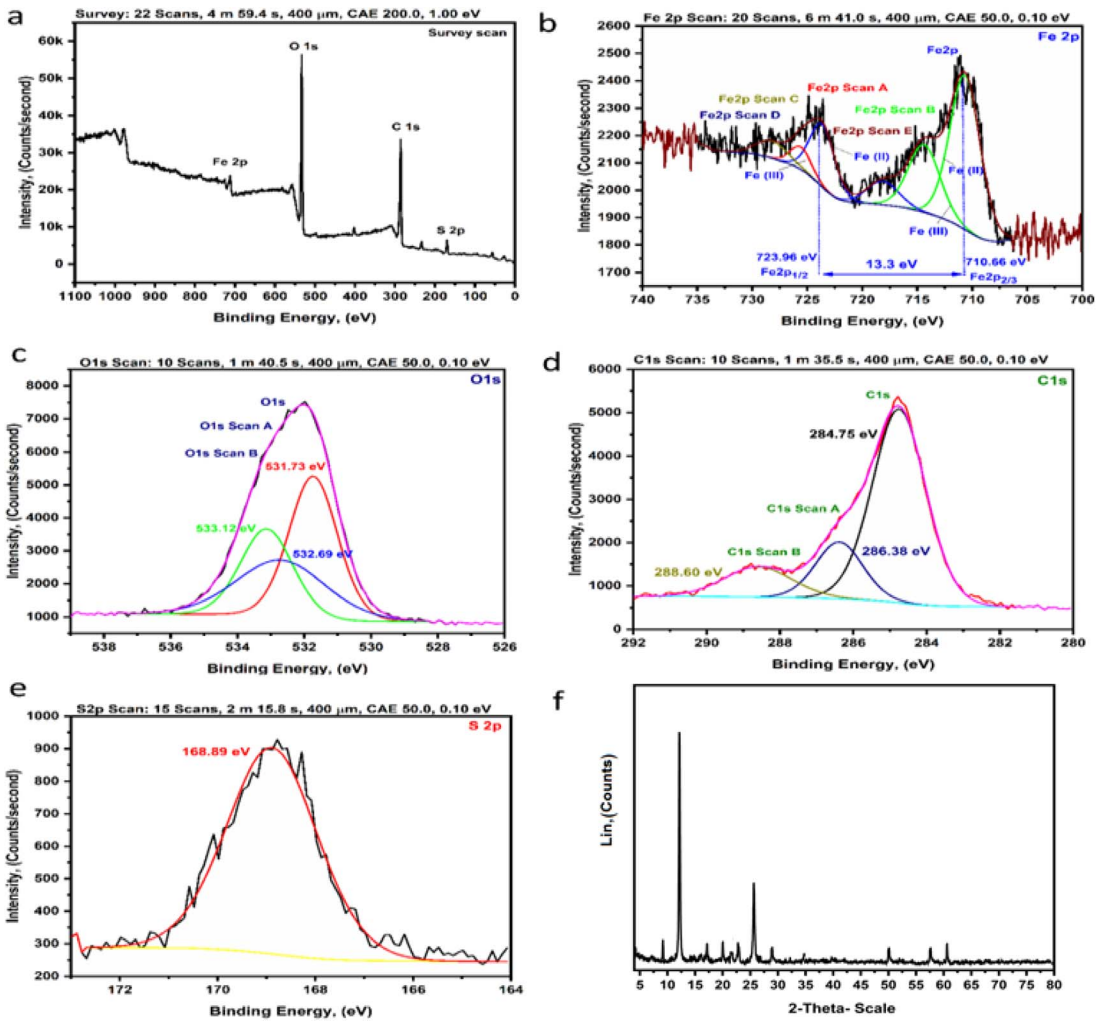

Fig. 5 (a–e) The XPS analysis of the Fe(III)–GA–MOF: [(a) survey, (b) Fe 2p, (c) O 1s, (d) C 1s, (e) S 2p], (f) the X-ray diffraction spectra of the Fe(III)–GA–MOF.

3.2.4. FT-IR spectrum. The FT-IR of CMC membrane (spectrum 1), MCMC membrane (spectrum 2), Fe–GA MOF (spectrum 3 and ESI S1.5†) and Fe–GA MOF embedded in MCMC thin film (spectrum 4) were presented in Fig. 6. The spectrum (Fig. 6, spectrum 1) displays peaks characteristic of cellulosic functional groups such as O–H (hydrogen bond) expansion at 3200–3400 cm^{-1}. The band at 1487 cm^{-1} in the spectra indicates the OH-bending in the adsorbent water. The ranges around 1467 cm^{-1} and 1325 cm^{-1} are assigned to CH_2 shear and OH-bending vibration. Furthermore, the infrared spectra display the presence of the carboxyl group, C=O at 1622–1637 cm^{-1}. According to Pecsok *et al.* (1976), the carboxylate groups and their salts show two peaks at wave number around 1600–1640 cm^{-1} and 1400–1450 cm^{-1} which symbolize the presence of a substituted carboxymethyl.[34] The band at 2920 cm^{-1} was due to C–H stretching where absorption at 1407 cm^{-1} reflects C–O–C curvature. The range 1017 cm^{-1} indicates the C–O stretching vibration. Running CMC generates many bands marked by epoxy groups. The MCMC spectrum (Fig. 6, spectrum 2) shows a significant increase in the methylene vibration band at 2862 cm^{-1} and the C–O–C stretching band of the oxirane group of the C–O–C band at 1078 cm^{-1} the stretching band of the C–O of the oxirane group at 961 cm^{-1}.[35,36] The FT-IR spectrum of Fe(III)–GA–MOF was shown in (Fig. 6, spectrum 3) in comparison with the FT-IR spectrum of GA (Fig. 6, inset). It can be concluded that: the main characteristic bands of gallic acid appeared for the hydroxyl (O–H) stretched at 3407.05 and 3269.11 cm^{-1} [phenol ν(OH) at 3407.05 cm^{-1} and carboxylate ν(OH) at 3269.11 cm^{-1}], and C=O and extends at 1612.39 cm^{-1}.[37] In addition to other major peaks that appeared at 3064.91, 2654.68, 1540.11, 1438.27, 1200.67, 1100.09, 1045.14, 762.25, 699.25, 567.87, 553.80, 466.88 cm^{-1}.[38] Characteristic bands of O–H and aromatic C–H axial distortion were exhibited near 3200 cm^{-1} and 3100 cm^{-1}, respectively. While C=O and C=C axial distortion were responsible for appearance of bands at 1700 cm^{-1} and in aromatics around 1600 and 1500 cm^{-1}, respectively. While the band at 1350 cm^{-1} indicated an O–H distortion; 1250 cm^{-1} C–O axial distortion and 650 cm^{-1} C–H axial distortion in aromatics. On the other hand, it was observed that the Fe(III)–GA–MOF FT-IR spectrum displayed hydroxyl (O–H) bands (phenol ν(OH) at 3407.05 cm^{-1} and carboxylate ν(OH)) at 3269.11 cm^{-1}) are due to complexation with iron ion. The coordination potentials of the iron ion and the gallic acid occur through the phenolic and carboxyl hydroxyl groups. With the formation of Fe(III)–GA–MOF and complexation with iron, a decrease in the intensity of the GA bands is observed. The decrease in peak intensity due to complexation with transition metals, metal ions can accept both electrons from the ligand as well as electrons from the aromatic ring when filling the d orbitals available for coordination. In contrast, no variations in the peaks located between 1200 and 720 cm^{-1} were detected for the angular distortions of the C–H bonds in the aromatic ring. The band shown at 590.85 and 476.79 cm^{-1} is for the coordination of ferric ions and oxygen and the covalent bonding [ν(Fe–O)] and [(Fe < –O)], respectively. The last two bars above assured the chelation of the ferric ion with GA by O atoms.[39] In view of the physical and spectroscopic results discussed in the above, the structure of Fe(III)–GA–MOF is in agreement with the previous published papers.[40–43] The FT-IR of MCMC membrane embedded Fe–GA MOF is presented in (Fig. 6, spectrum 4). The spectrum displays peaks characteristic of cellulosic functional groups such as O–H (hydrogen bond) expansion at 3200–3400 cm^{-1}, the band at 1487 cm^{-1} in the spectra indicates the OH-bending in the adsorbent water and peaks characteristics to Fe–GA MOF such as Fe–O (metal–oxygen bond) at 590.85 and 476.79 cm^{-1}.

3.2.5. TGA of Fe–gallic acid MOF embedded in epoxy-functionalized carboxymethyl cellulose polymer thin film. The TGA results were presented in Fig. 7. The TGA results (line A) for functionalized epoxy cellulose polymer with epichlorohydrin typically show a two-step degradation process. The first step, which occurs at a temperature of 200–300 °C, is due to the decomposition of the epoxy groups. The second step, which occurs at a temperature of 400–500 °C, is due to the

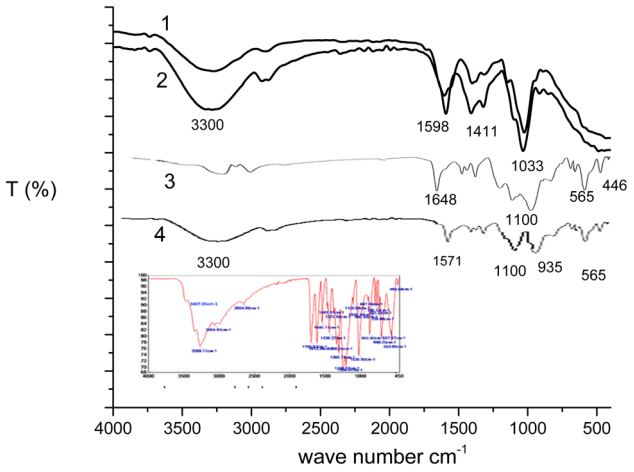

Fig. 6 The FT-IR spectra of (1) CMC, (2) its epoxy derivative (MCMC), (3) Fe(III)–GA–MOF and (4) Fe(III)–GA–MOF embedded in epoxy derivative (MCMC) (inset: FT-IR spectrum of GA).

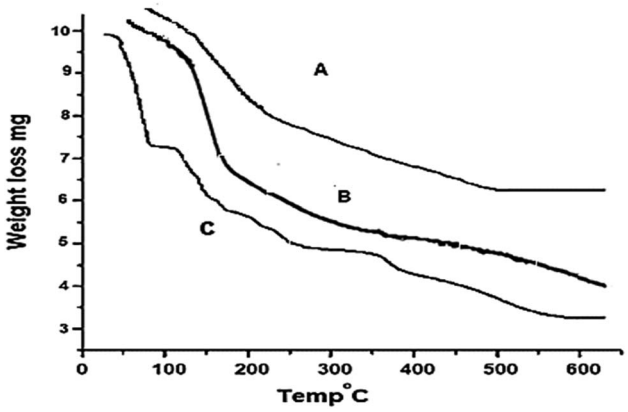

Fig. 7 TGA of (A) epoxy-functionalized carboxymethyl cellulose polymer, (B) epoxy-functionalized carboxymethyl cellulose polymer thin film and (C) epoxy-functionalized carboxymethyl cellulose polymer thin film/CA 15-3 antigen.

decomposition of the cellulose. The functional groups do not significantly affect the thermal stability of the polymer. The TGA (line B) of functionalized epoxy cellulose polymer with epichlorohydrin sensor toward temperature shows a two-step degradation process. The first step, which occurs at a temperature of 200–300 °C, is due to the decomposition of the epoxy groups. The second step, which occurs at a temperature of 400–500 °C, is due to the decomposition of the cellulose. The TGA (line C) epoxy cellulose doped CA 125 antigen showed that the decomposition in three well-defined steps. The first step is the decomposition occurred in the range 60–150 °C due to loss of water incorporated in the substrate polymer. The second step is the degradation occurs at a temperature of 200–300 °C, and is due to the unfolding and denaturation of the antigen protein. The third step is weight loss at the temperature of 400–500 °C is due to the decomposition of the cellulose.

3.3. Spectral characteristics

MOFs composed of gallic acid (GA) ligands show luminescence/sensing properties due to their conjugate systems with low energy LUMO (p*) of GA bond, thus, GA-based MOFs are effective for sensing. Furthermore, because of their free core sites, the host frameworks owe the capabilities of performing the fluorophore role efficiently and interacting selectively with the targeted analyte. Once the analyte was sensed by the receptor, fluorescence signals could be detected by either electron, energy or charge transfer mechanisms. It is hard for M^{2+} ion to be oxidized or reduced through d^{10} formation, primarily resulting in localized ligand emission induced by p–p* and/or n–p* transitions of the conjugate ligands. On the other hand, the participation of metal/ligand and ligand/ligand charge transfer in emission were considered to be negligible. Hence, the metal complex's luminescent emission band could be attributed to intra-ligand emission. While luminescence intensity enhancement was assigned to the coordination bonds between the M^{2+} and the ligand that tuned the ligand's conformational stiffness and led to a reduction in the non-radiative transmission. Regarding M^{3+} possessing paramagnetic properties (Fe^{3+}, d^5), the metal/ligand or metal/metal bonding charge transfer contribution are considered to be predominant in the emission process. Weak emission is typically seen in complexes of paramagnetic transition metals. Whereas their partially filled orbitals, producing d–d ligand domain transitions, might strongly promote the readsorption and/or fluorescence quenching of organic molecules through electron or energy transfer. The nature of MOFs structure greatly affected the emissivity.[44,45] Most often, the luster of MOFs comprising transition metals is based on the linker, but yet can entail metal ion disorder on the linkers or make charge transfer between the linker and the metal.[46] The emission spectra of gallic acid its main peak at 409 nm that could be assigned to the p*–p transition as presented in Fig. 8a.[47] Fe–GA framework showed emission at 420 nm (λ_{ex} = 350 nm) when complexed with Fe^{3+} as presented in Fig. 8a. The emission spectrum of Fe–GA MOF embedded in epoxy cellulose polymer is shown in Fig. 8b, the spectrum shows a band at 439 nm in

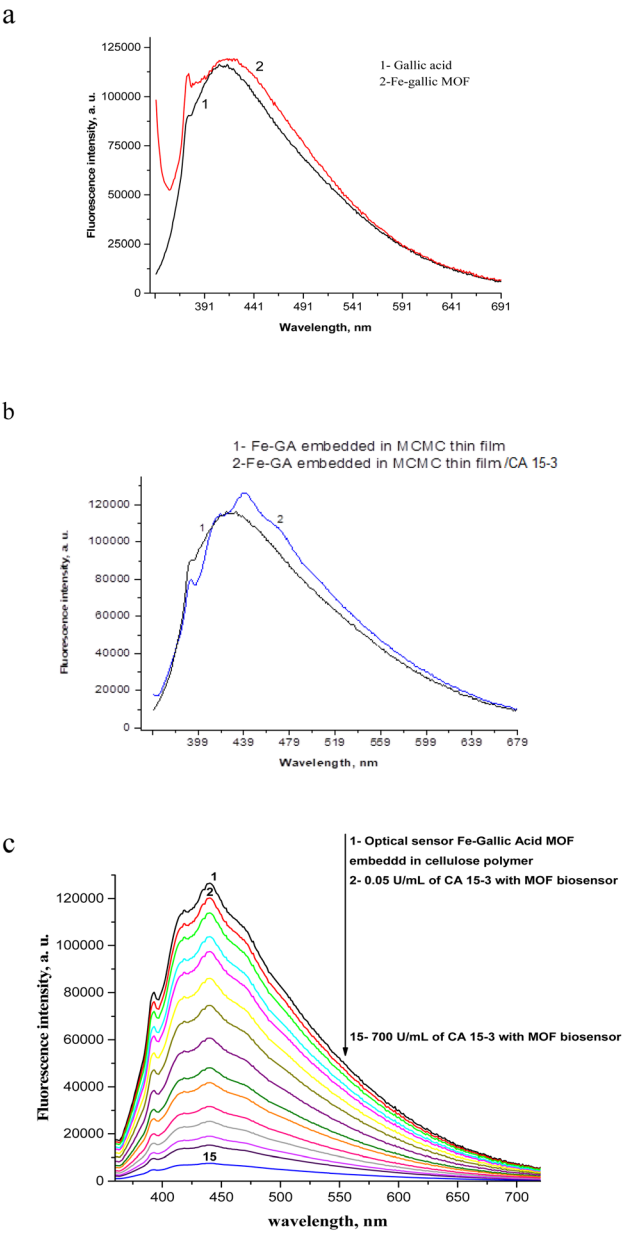

Fig. 8 Emission spectra of the gallic acid and Fe–gallic acid (a), emission spectra of thin film containing Fe–GA embedded in epoxy cellulose polymer and thin film containing Fe–GA embedded in epoxy cellulose polymer (b), emission spectra of thin film containing Fe–GA embedded in epoxy cellulose polymer in different CA 15-3 concentrations (c) at λ_{ex} = 350 nm.

which a red shift by 19 nm for the fluorescence spectrum of Fe–GA MOF. After addition of different concentrations of CA 15-3 to the thin fim embedded Fe–GA MOF, the quenching takes place for the band at 439 nm, Fig. 8c. The stability of biomolecules at room temperature is a major drawback of biosensors. This is because biomolecules are often sensitive to heat, light, and other environmental factors. As a result, they can degrade or lose their activity over time.[48,49] The Fe–gallic acid doped in epoxy cellulose polymer sensor is a new type of biosensor that has been shown to be more stable than traditional biosensors. This is because the Fe–gallic acid doped in epoxy cellulose

polymer provides a protective environment for the biomolecules. The Fe–gallic acid doped in epoxy cellulose polymer also helps to prevent the biomolecules from degrading or losing their activity.[50] In addition, the Fe–gallic acid doped in epoxy cellulose polymer sensor is more stable at room temperature than traditional biosensors. This is because the Fe–gallic acid doped in epoxy cellulose polymer helps to prevent the biomolecules from being damaged by heat. As a result of these factors, the Fe–gallic acid doped in epoxy cellulose polymer sensor can be used to transport and handle biomolecules at room temperature for extended periods. This makes it a valuable tool for a variety of applications, including clinical diagnostics and environmental monitoring.

4. Validation

4.1. Calibration curve

1.5 mL of different CA 15-3 standard solutions over concentration range of 0.05–570 U mL^{-1} was added to the thin film embedded Fe–gallic acid MOF in the fluorimeter cell. The spectra of luminescence were recorded at 439 nm (λ_{em}) and a calibration graph was constructed between $(F_0/F - 1)$ and the corresponding concentrations of CA 15-3 as displayed in Fig. 9 after application of Stern–Volmer plot;[51–68] $(F_0/F) - 1 = \kappa_{sv}$ [CA 15-3] where κ_{sv} (Stern–Volmer constant) and [CA 15-3] is the quencher concentration. The critical concentration (C_0) at which the intensity of the biosensor is reduced to half value. κ_{sv} and $C_0 = (1/\kappa_{sv})$ are calculated to be 0.01 U mL^{-1} and 100 U mL^{-1}, respectively. R_0 is the critical transfer distance, which is the average distance between the donor and the acceptor at which the probability of fluorescence quenching is just equal to 0.5 excited state, $R_0 = 7.35/(C_0)^{1/3} = 1.58$ Å, indicating the quenching mechanism is a dynamic quenching through an electron transfer mechanism. The given method proved favorable sensitivity by virtue of the LOD 0.01 U mL^{-1} and LOQ 0.03 U mL^{-1} values and the appropriate working range of 0.05–570 U mL^{-1} as shown in Table 1.

4.2. Accuracy and precision

The accuracy of the presented optical method was estimated as percentage relative error (%RE) for the measured mean CA 15-3 concentration and the respective actual concentration. The recovery assays were achieved *via* selecting two CA 15-3 concentrations; 150 and 300 units per mL in addition to one real sample, see Table 2. The concentrations of the selected samples were determined employing both the proposed and the

Table 1 Sensitivity and regression parameters for photo probe

Parameter	Value
λ_{em} (nm)	439
Linear range (U mL^{-1})	0.05–570
Limit of detection (LOD) (U mL^{-1})	0.02
Limit of quantification (LOQ) (U mL^{-1})	0.06
Regression equation (Y^a)	$Y = bX$
Intercept (a)	0.001
Slope (b)	0.01
Standard deviation $\times 10^{-4}$	1.0
Regression coefficient (r)	0.998

[a] Where $Y = [(F_0/F) - 1]$, X = concentration in mol L^{-1}, a = intercept, b = slope.

Table 2 Results of recovery study using standard and proposed methods

Samples	CA 15-3 (U mL^{-1})	Found CA 15-3	Pure CA 15-3 recovered (percent ± SD)
Sample 1	150	150.8	100.53 ± 2.8
Sample 2	300	298	99.33 ± 2.5
Serum sample containing CA 15-3	47[a]	48.5	103.19 ± 1.5

[a] This value was obtained by ELISA for determination of the serum sample of patient.

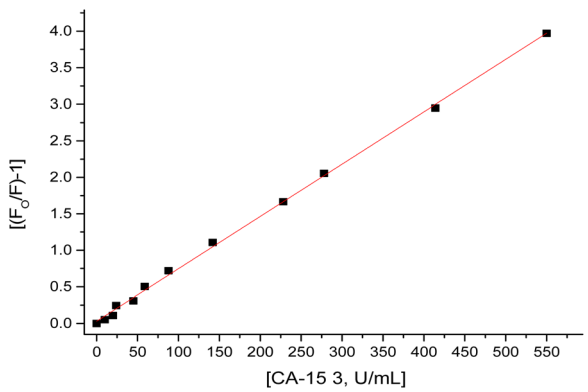

Fig. 9 Linear relationship between $[(F_0/F) - 1]$ against [CA 15-3].

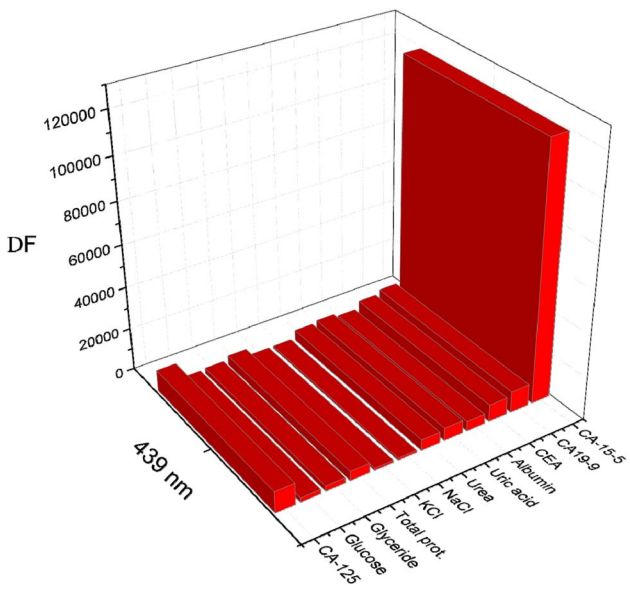

Fig. 10 Effect of interfering species on the fluorescence intensity of the optical biosensor.

Table 3 Evaluation of intra-day and inter-day accuracy and precision

	Standard method	Propose method					
		Intra-day accuracy and precision ($n = 3$)			Inter-day accuracy and precision ($n = 3$)		
Sample	Average (U mL^{-1})[36]	Average found (U mL^{-1} ± CL)	%RE	%RSD	Average found (U mL^{-1} ± CL)	%RE	%RSD
Sample (1)	350.0	353.5 ± 11.24	1.00	1.278	355.3 ± 11.06	1.50	1.272
Sample (2)	9.910	10.03 ± 0.365	1.20	1.465	10.08 ± 0.359	1.70	1.458
Sample (3)	20.30	20.90 ± 1.233	3.00	2.372	20.64 ± 1.213	1.70	2.402
Sample (3)	480.0	484.8 ± 15.42	1.00	1.278	487.2 ± 15.17	1.50	1.272
Sample (5)	0.950	0.959 ± 0.029	1.00	1.250	0.964 ± 0.029	1.50	1.244
Sample (6)	155.0	156.5 ± 4.974	1.00	1.277	157.3 ± 4.894	1.50	1.271
Sample (7)	1.540	1.555 ± 0.047	1.00	1.221	1.563 ± 0.046	1.50	1.215
Sample (8)	0.400	0.405 ± 0.014	1.40	1.479	0.407 ± 0.014	1.90	1.472
Sample (9)	4.970	5.019 ± 0.159	1.00	1.274	5.044 ± 0.156	1.50	1.268
Sample (10)	88.50	89.38 ± 2.842	1.00	1.278	89.82 ± 2.797	1.50	1.272
Sample (11)	225.5	232.3 ± 12.86	3.00	2.227	228.2 ± 12.66	1.20	2.267
Sample (12)	500.0	497.5 ± 10.17	−0.50	0.822	495 ± 10.01	−1.00	0.826
Sample (13)	48.50	48.98 ± 1.557	1.00	1.277	49.22 ± 1.532	1.50	1.271
Sample (14)	132.7	134.0 ± 4.263	1.00	1.278	134.7 ± 4.194	1.50	1.272
Sample (15)	287.5	284.3 ± 9.526	−1.10	1.346	283.2 ± 9.373	−1.50	1.352

reference method[69] and the results were summarized in Table 2 showing no significant difference between the two methods. Regarding the precision of the method, both intra and inter-day precision were evaluated through determining 15 samples of different CA 15-3 concentrations in triplicates within the same day and on three consecutive days. The acquired data were processed and the values of % relative standard deviation assured the high precision of the proposed biosensor as presented in Table 2.

4.3. Selectivity

This method has high selectivity for CA 15-3 in the presence of all interfering species within the blood sample due to the specific interaction between CA 15-3 in blood samples with Fe–gallic acid embedded in the thin film. The influence of potential interfering compounds on the luminescence spectra of the CA 15-3 optical biosensor was investigated to assess the method's selectivity. The interfering compounds involved in the study were sodium and potassium chloride in concentration 2.0×10^{-3} mol L^{-1}, urea and triglycerides in concentration of 0.06 g L^{-1}, uric acid and glucose in concentration of 0.08 g L^{-1}, albumin and total protein in concentration of 0.7 g L^{-1} and 0.01 g L^{-1}, respectively. Furthermore, other the effect of other related tumor markers for breast cancer was studied, where CA 125, CA 19-9 and CEA, 200 U mL^{-1} each were included in the study. All of the examined interfering compounds showed negligible impact on the optical probe in presence of CA 15-3 in concentration of 150 U mL^{-1}. The impact of interfering compounds on the photo probe was illustrated in Fig. 10.

4.4. Application to real samples

The newly suggested optical sensor was employed to determine CA 15-3 in serum samples of patient and healthy humans. The results in Table 3 showed the success of the method in determining CA 15-3 in serum samples. The utility of the proposed analytical method was examined through determining CA-15-3 concentration in different serum samples, 5 samples from healthy status and 10 samples from breast cancer patients of breast cancer in the age range from 30 to 50 years. Good agreement between the average values obtained by the developed procedure (0.408–10.07 ± 1.215–1.472 U mL^{-1}), (20.9–495 ± 0.83–2.14 U mL^{-1}) and the standard method (0.4–9.9 ± 1.25–1.48 U mL^{-1}), (20.3–500 ± 0.83–1.5 U mL^{-1}) for healthy and breast cancer serum samples, respectively, and no significant differences were found for the two methods, Table 3. CA 15-3 evaluation as a biomarker for prognosis of breast malignancy employing the proposed optical biosensor enhanced the sensitivity and specificity of the biomarker; sensitivity = 93.33%, specificity = 91.6%, positive predictive value = 93.33%, negative predictive value = 91.6% and prevalence disease = 57.7%.

5. Conclusion

The presented luminescent strategy based on the use of the Fe–gallic acid MOF optical sensor doped in a cellulose polymer is a promising new method for the quantification of CA 15-3 in serum of breast cancer women. The method is simple, cost-effective, and sensitive. It has the potential to be a valuable tool for the diagnosis and monitoring of breast cancer. The LOD of 0.02 U mL^{-1} is significantly lower than the LOD of other published determination methods. This means that the Fe–GA MOF sensor is able to detect CA 15-3 at much lower concentrations. This is important because it allows for the early detection of breast cancer, which is essential for successful treatment. The Fe–GA MOF sensor is also more sensitive to CA 15-3 in water than in other solvents. This is because the MOF is able to interact with water molecules in a way that enhances its sensitivity to CA 15-3. This makes the sensor ideal for use in serum samples, which are mostly water.

Conflicts of interest

The authors declare no conflict of interest.

Acknowledgements

Authors extend their appreciation to the Deputyship for Research & Innovation, Ministry of Education in Saudi Arabia for funding this research work through the project number "NBU-FFR-2023-0051".

References

1 A. Elzagheid, T. Kuopio, S. Pyrhonen and Y. Collan, *Diagn. Pathol*, 2006, **1**, 41.
2 C. Tondini, D. F. Hayes and D. W. Kufe, *Hematol. Oncol. Clin. North Am.*, 1989, **3**, 653.
3 Noha M. Said, *Mol. Biol. Rep.*, 2019, **46**, 2013.
4 X. Hing, C. W. Mok, P. T. Tan, S. S. Sudhakar, C. M. Seah, W. P. Lee and S. M. Tan, *Breast*, 2020, **52**, 95.
5 R. Rashed, H. Darwish, M. Omran, A. Belal and F. Zahran, *Br. J. Biomed. Sci.*, 2020, **77**, 196.
6 M. J. Duffy, D. Evoy and E. W. M. Dermott, *Clin. Chim. Acta*, 2010, 1869.
7 N. Benjamin, M. Ofra, A. Tanir, K. Luna, M. Bella, H. Tamar and P. Tamar, *Anticancer Res.*, 2013, **33**, 293.
8 F. M. T. Agyei, E. Darko and A. B. Wiafe, *Pak. J. Biol. Sci.*, 2008, **11**, 1945.
9 T. T. Bekci, T. Senol and E. Maden, *J. Int. Med. Res.*, 2009, **37**, 438.
10 W. Wang, S. Li, G. Zhang, J. He and Z. Ma, *Int. J. Electrochem. Sci.*, 2017, **12**, 10791.
11 L. Zhang, Y. He, H. Wang, Y. Yuan, R. Yuan and Y. Chai, *Biosens. Bioelectron.*, 2015, **74**, 924.
12 H. Li, J. He, S. Li and A. Turner, *Biosens. Bioelectron.*, 2013, **43**, 25.
13 X.-B. Cheng, C.-Z. Zhao, Y.-X. Yao, H. Liu and Q. Zhang, Recent advances in energy chemistry between solid-state electrolyte and safe lithium-metal anodes, *Chem*, 2019, **5**, 74–96.
14 A. Kirchon, L. Feng, H. F. Drake, E. A. Joseph and H.-C. Zhou, From fundamentals to applications: a toolbox for robust and multifunctional MOF materials, *Chem. Soc. Rev.*, 2018, **47**, 8611–8638.
15 M. S. Attia, A. O. Youssef, M. N. Abou-Omar, E. H. Mohamed, R. Boukherroub, A. Khan, T. Altalhi and M. A. Amin, Emerging advances and current applications of nano MOF-based membranes for water treatment, *Chemosphere*, 2022, **292**, 133369.
16 F. Yan, X. Wang, Y. Wang, C. Yi, M. Xu and J. Xu, Sensing performance and mechanism of carbon dots encapsulated into metal–organic frameworks, *Microchim. Acta*, 2022, **189**, 379.
17 G. Harine, V. M. Ajay, P. Rajkumar and R. S. Bhaskar, Metal–organic framework derived carbon-based electrocatalysis for hydrogen evolution reactions: a review, *Mater. Today Sustainability*, 2023, **22**, 100371.
18 H.-Q. Yin and X.-B. Yin, Metal–organic frameworks with multiple luminescence emissions: designs and applications, *Acc. Chem. Res.*, 2020, **53**, 485–495.
19 X. Xu, M. Ma, T. Sun, X. Zhao and L. Zhang, Luminescent guests encapsulated in metal–organic frameworks for portable fluorescence sensor and visual detection applications, *Biosensors*, 2023, **13**, 435.
20 S. Kundu, A. K. Swaroop and J. Selvaraj, Metal–organic framework in pharmaceutical drug delivery, *Curr. Top. Med. Chem.*, 2023, **23**(13), 1155–1170.
21 B. Li, J.-P. Dong, Z. Zhou, R. Wang, L.-Y. Wang and S.-Q. Zang, Robust lanthanide metal–organic frameworks with "all-in-one" multifunction: efficient gas adsorption and separation, tunable light emission and luminescence sensing, *J. Mater. Chem. C*, 2021, **9**, 3429–3439.
22 H. Kaur, S. Sundriyal, V. Pachauri, S. Ingebrandt, K.-H. Kim, A. L. Sharma and A. Deep, Luminescent metal–organic frameworks and their composites: potential future materials for organic light emitting displays, *Coord. Chem. Rev.*, 2019, **401**, 213077.
23 W. P. Lustig and J. Li, Luminescent metal–organic frameworks and coordination polymers as alternative phosphors for energy efficient lighting devices, *Coord. Chem. Rev.*, 2018, **373**, 116–147.
24 J. Dong, D. Zhao, Y. Lu and W.-Y. Sun, Photoluminescent metal–organic frameworks and their application for sensing biomolecules, *J. Mater. Chem. A*, 2019, **7**, 22744–22767.
25 Y. Zhang, S. Yuan, G. Day, X. Wang, X. Yang and H.-C. Zhou, Luminescent sensors based on metal–organic frameworks, *Coord. Chem. Rev.*, 2018, **354**, 28–45.
26 R. Hardian, S. Dissegna, A. Ullrich, P. L. Llewellyn, M.-V. Coulet and R. A. Fischer, Tuning the properties of MOF-808 *via* defect engineering and metal nanoparticle encapsulation, *Chem.–Eur. J.*, 2021, **27**, 6804–6814.
27 X. Liu, H. Hu, Y. Liu, Z. Huang, Y. Lu, X. Zhou and J. Wang, Experimental investigation on fluorescence polarization properties of isomerical MOF/T RhB crystals, *J. Solid State Chem.*, 2020, **284**, 121179.
28 L. Qiu, C. Yu, X. Wang, Y. Xie, A. M. Kirillov, W. Huang, J. Li, P. Gao, T. Wu, X. Gu, *et al.*, Tuning the solid–state white light emission of postsynthetic lanthanide-encapsulated double-layer MOFs for three-color luminescent thermometry applications, *Inorg. Chem.*, 2019, **58**, 4524–4533.
29 M. S. Attia, A. A. Mohamed, M. M. El-Saady, M. N. Abou-Omar, H. G. Afify, T. A. Amin, A. H. Hosny, A. O. Youssef and M. S. Mohy-Eldind, A new method for early diagnosis of liver cancer using a biosensor embedded in an alginate polymer thin film, *J. Mater. Chem. C*, 2022, **10**, 6464–6472.
30 T. Manjuraj, G. Krishnamurthy, Y. D. Bodke and H. S. Bhojya Naik, *J. Mol. Struct.*, 2017, **1148**, 231–237.
31 R. Sacourbaravi, Z. Ansari, A. Mohammad, K. Valiollah and N. Esmaeil, Fabrication of Ag NPs/Zn-MOF nanocomposites and their application as antibacterial agents, *J. Inorg. Organomet. Polym. Mater.*, 2020, **30**, 4615–4621, DOI: **10.1007/s10904-020-01601-x**.

32 A. Barhoum, G. Van Assche, A. S. H. Makhlouf, H. Terryn, K. Baert, M.-P. Delplancke, S. M. El-Sheikh and H. Rahier, A green, simple chemical route for the synthesis of pure nanocalcite crystals, *Cryst. Growth Des.*, 2015, **15**, 573–580.

33 (*a*) H. Niu, Y. Zheng, S. Wang, S. He and Y. Cai, Stable hierarchical microspheres of 1D Fe–gallic acid MOFs for fast and efficient Cr(VI) elimination by a combination of reduction, metal substitution and coprecipitation, *J. Mater. Chem. A*, 2017, **5**, 16600; (*b*) M. A. Rahim, K. Kempe, M. Mullner, H. Ejima, Y. Ju, M. P. van Koeverden, T. Suma, J. A. Braunger, M. G. Leeming, B. F. Abrahams and F. Caruso, Surface-confined amorphous films from metal-coordinated simple phenolic ligands surface-confined amorphous films from metal-coordinated simple phenolic ligands, *Chem. Mater.*, 2015, **27**, 5825.

34 P. R. Satheesh Chandran, U. S. Soumya Mol, R. Drisya, M. R. Sudarsanakumar and M. R. Prathapachandra Kurup, *J. Mol. Struct.*, 2017, **1137**, 396–402.

35 A. A. Jadhav, V. P. Dhanwe and P. K. Khanna, *Polyhedron*, 2017, **123**, 99–110.

36 Y. S. Yang, M. Liu, Y. P. Yang, Q. H. Jin, Z. F. Li, X. N. Xue, Z. J. Zhang and W. J. Zheng, *Polyhedron*, 2015, **93**, 66–75.

37 R. L. Pescok, L. D. Shields, T. Caims and I. G. McWilliam, *Modern Methods of Chemical Analysis*, Wiley, New York, 1976.

38 R. P. Paitandi, R. S. Singh, S. Mukhopadhyay, G. Sharma, B. Koch, P. Vishnoi and D. S. Pandey, *Inorg. Chim. Acta*, 2017, **454**, 117–127.

39 A. Vlad, M. F. Zaltariov, S. Shova, M. Cazacu, M. Avadanei, A. Soroceanu and P. Samoila, *Polyhedron*, 2016, **115**, 76–85.

40 Ahmed E. Fazary, M. Taha and Yi-H. Ju, Iron complexation studies of gallic acid, *J. Chem. Eng. Data*, 2009, **54**(1), 35–42.

41 L. Levy, A. Gurov and A. Radian, The effect of gallic acid interactions with iron-coated clay on surface redox reactivity, *Water Res.*, 2020, **184**(1), 116190.

42 F. Frešer, G. Hostnik, J. Tošović and B. Urban, Dependence of the Fe(II)–gallic acid coordination compound formation constant on the pH, *Foods*, 2021, **10**(11), 2689.

43 Li-li Lu, Y.-hua Li and X.-yang Lu, Kinetic study of the complexation of gallic acid with Fe(II), *Spectrochim. Acta, Part A*, 2009, **74**(3), 829–834.

44 J. Guo, J. F. Ma, J.-J. Li, J. Yang and S.-X. Xing, *Cryst. Growth Des.*, 2012, **12**, 6074–6082.

45 M. Zheng, H. Tan, Z. Xie, L. Zhang, X. Jing and Z. Sun, *ACS Appl. Mater. Interfaces*, 2013, **5**, 1078–1108.

46 M. D. Allendorf, C. A. Bauer, R. K. Bhakta and R. J. T. Houk, *Chem. Soc. Rev.*, 2009, **38**, 1330.

47 M. S. Attia, A. O. Youssef, Z. A. Khan and M. N. Abou-Omar, *Talanta*, 2018, **186**, 36–43.

48 J. Yoon, M. Shin, T. Lee and J.-W. Choi, *Materials*, 2020, **13**(2), 299.

49 K. Theyagarajan and Y.-J. Kim, *Biosensors*, 2023, **13**(4), 424.

50 H. N. Abdelhamid and A. P. Mathew, *Coord. Chem. Rev.*, 2022, **451**, 214263.

51 M. S. Attia and N. S. Al-Radadi, *Biosens. Bioelect.*, 2016, **86**, 413–419.

52 M. S. Attia, M. H. Khalil, M. S. A. Abdel-Mottaleb, M. B. Lukyanova, Y. A. Alekseenko and B. Lukyanov, *Int. J. Photoenergy*, 2006, 1–9.

53 M. S. Attia, A. O. Youssef and A. A. Essawy, *Anal. Methods*, 2012, **4**, 2323–2328.

54 M. S. Attia, K. Ali, M. El-Kemary and W. M. Darwish, *Talanta*, 2019, **201**, 185–193.

55 M. S. Attia, W. H. Mahmoud, A. O. Youssef and M. S. Mostafa, *J. Fluoresc.*, 2011, **21**, 2229–2235.

56 M. S. Attia, M. N. Ramsis, L. H. Khalil and S. G. Hashem, *J. Fluoresc.*, 2012, **22**, 779–788.

57 M. S. Attia, W. H. Mahmoud, M. N. Ramsis, L. H. Khalil, A. M. Othman, S. G. Hashem and M. S. Mostafa, *J. Fluoresc.*, 2011, **21**, 1739–1748.

58 M. S. Attia, A. M. Othman, E. Elraghi and H. Y. Aboul-Enein, *J. Fluoresc.*, 2011, **21**, 739–745.

59 A. A. Elabd and M. S. Attia, *J. Lumines.*, 2016, **169**, 313–318.

60 M. S. Attia, E. Bakir, A. A. Abdel-Aziz and M. S. A. Abdel-Mottaleb, *Talanta*, 2011, **84**, 27–33.

61 M. S. Abdel-Wahed, A. S. El-Kalliny, M. I. Badawy, M. S. Attia and T. A. Gad-Allah, *Chem. Eng. J.*, 2020, **382**, 122936.

62 M. S. Attia, S. A. Elsaadany, K. A. Ahmed, M. M. El-Molla and M. S. A. Abdel-Mottaleb, *J. Fluoresc.*, 2015, **25**, 119–125.

63 S. G. Hashem, M. M. Elsaady, H. G. Afify, M. El-Kemary and M. S. Attia, *Talanta*, 2019, **199**, 89–96.

64 M. S. A. Abdel-Mottaleb, M. Saif, M. S. Attia, M. M. Abo-Aly and S. N. Mobarez, *Photochem. Photobiol. Sci.*, 2018, **17**, 221–230.

65 W. E. Omer, M. A. El-Kemary, M. M. Elsaady, A. A. Gouda and M. S. Attia, *ACS Omega*, 2020, **5**, 5629–5637.

66 L. M. Abdullah, M. S. Attia and M. S. A. Abdel-Mottaleb, *Energy J. Chem.*, 2019, **62**, 247–255.

67 M. S. Attia, A. O. Youssef, A.-S. S. H. Elgazwy, S. M. Agami and S. I. Elewa, *J. Fluoresc.*, 2014, **24**, 759–765.

68 ICH, *Validation of Analytical Procedures: Text and Methodology, Q2(R1), Complementary Guideline on Methodology*, London, ICH, 1996, Incorporated in 2005.

69 L. Harris, et al., American society of clinical oncology (2007) update of recommendations for the use of tumor markers in breast cancer, *J. Clin. Oncol*, 2007, **25**(33), 5287–5312.